

Confined Lithium–Sulfur Reactions in Narrow-Diameter Carbon Nanotubes Reveal Enhanced Electrochemical Reactivity

Chengyin Fu,[†] M. Belén Oviedo,[†] Yihan Zhu,[‡] Arthur von Wald Cresce,[#] Kang Xu,[#] Guanghui Li,^{†,‡} Mikhail E. Itkis,^{†,‡,§} Robert C. Haddon,^{†,‡,§} Miaofang Chi,[○] Yu Han,[▽] Bryan M. Wong,^{*,†,||} and Juchen Guo^{*,†,||}

[†]Department of Chemical and Environmental Engineering, [‡]Center for Nanoscale Science and Engineering, [§]Department of Chemistry, and ^{||}Materials Science and Engineering Program, University of California-Riverside, California 92521, United States

[‡]Department of Chemical Engineering, Zhejiang University of Technology, Hangzhou 310014, China

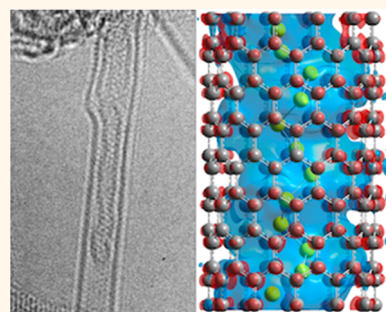
[#]United States Army Research Laboratory, Adelphi, Maryland 20783, United States

[○]Center for Nanophase Materials Sciences, Oak Ridge National Laboratory, Oak Ridge, Tennessee 37831, United States

[▽]Chemical Science Program, King Abdullah University of Science and Technology, Thuwal 23955, Kingdom of Saudi Arabia

Supporting Information

ABSTRACT: We demonstrate an unusual electrochemical reaction of sulfur with lithium upon encapsulation in narrow-diameter (subnanometer) single-walled carbon nanotubes (SWNTs). Our study provides mechanistic insight on the synergistic effects of sulfur confinement and Li⁺ ion solvation properties that culminate in a new mechanism of these sub-nanoscale-enabled reactions (which cannot be solely attributed to the lithiation–delithiation of conventional sulfur). Two types of SWNTs with distinct diameters, produced by electric arc (EA-SWNTs, average diameter 1.55 nm) or high-pressure carbon monoxide (HiPco-SWNTs, average diameter 1.0 nm), are investigated with two comparable electrolyte systems based on tetraethylene glycol dimethyl ether (TEGDME) and 1,4,7,10,13-pentaoxacyclopentadecane (15-crown-5). Electrochemical analyses indicate that a conventional solution-phase Li–S reaction occurs in EA-SWNTs, which can be attributed to the smaller solvated [Li(TEGDME)]⁺ and [Li(15-crown-5)]⁺ ions within the EA-SWNT diameter. In stark contrast, the Li–S confined in narrower diameter HiPco-SWNTs exhibits unusual electrochemical behavior that can be attributed to a solid-state reaction enabled by the smaller HiPco-SWNT diameter compared to the size of solvated Li⁺ ions. Our results of the electrochemical analyses are corroborated and supported with various spectroscopic analyses including *operando* Raman, X-ray photoelectron spectroscopy, and first-principles calculations from density functional theory. Taken together, our findings demonstrate that the controlled solid-state lithiation–delithiation of sulfur and an enhanced electrochemical reactivity can be achieved by sub-nanoscale encapsulation and one-dimensional confinement in narrow-diameter SWNTs.



KEYWORDS: lithium–sulfur battery, single-walled carbon nanotubes, sub-nanoscale confined sulfur, electrochemical systems, controlled solid-state reactions

Electrochemical reactions between lithium (Li) and sulfur (S) constitute the fundamental building blocks for enabling rechargeable Li–S battery chemistries. When sulfur is in its native cyclo-S₈ molecular state and ethers are used as the electrolyte solvents, a series of complex lithiation reactions occur in the electrolyte, generating Li polysulfides that ultimately result in the precipitation of lower-order polysulfides or lithium sulfide. The exact chemical fate and transport processes in these uncontrolled interfacial chemical environments are poorly understood to date, which pose fundamental challenges to improving Li–S batteries. As

an alternative strategy to controlling these chemical interactions, we have sought to shift the current Li–S electrochemical reaction paradigm from solution to the solid phase. Specifically, one of our previous studies suggested that the Li–S electrochemical mechanism is dictated by the geometry of the sulfur confinement,¹ and solid-state (or quasi-solid-state) Li–S electrochemical reactions could occur

Received: December 12, 2017

Accepted: September 24, 2018

Published: September 24, 2018

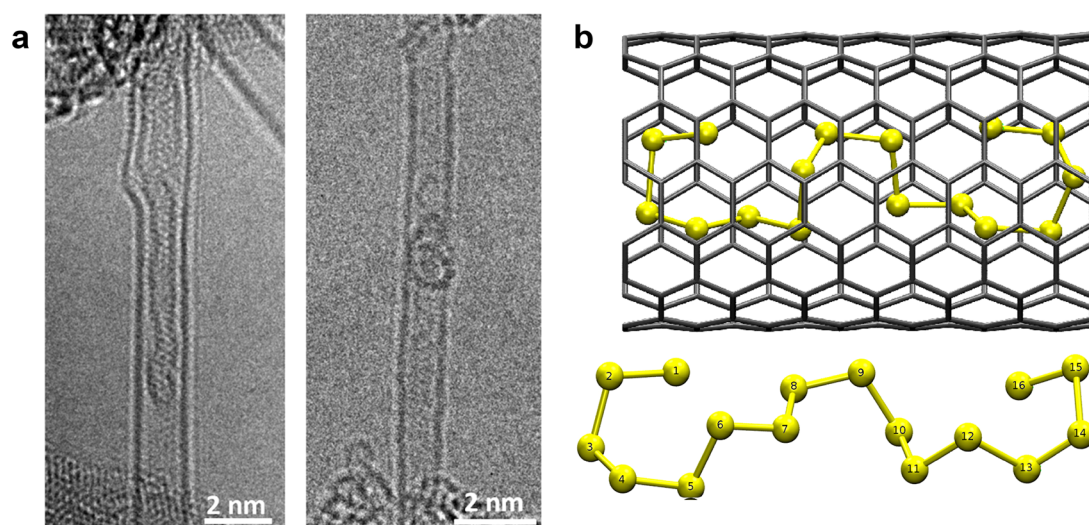


Figure 1. TEM images of (a) S@EA (left) and S@HiPco (right). (b) Optimized geometry of a sulfur chain inside a (7,7) SWNT (top) and view of the sulfur chain without the (7,7) SWNT (bottom). The diameter of the optimized S@(7,7)SWNT is 9.93 Å. The optimized total electronic energy is -1.6 keV, and the cohesive energy is -0.9 eV.

in liquid electrolytes by confining sulfur in subnanometer pores in microporous carbon. Due to the subnano pore size, solvated Li^+ ions enter the pores through a desolvation process so that solid-state or quasi-solid-state Li–S electrochemical reactions occur in this subnano confined environment. Similar solid-state Li–S electrochemical mechanisms enabled by subnanometer confinement were also proposed by the Gentle² and Huang³ groups, with other hypotheses including the existence of small sulfur allotropes in subnanometer confinements,⁴ carbon sulfurization,⁵ and formation of solid electrolyte interphase (SEI) on the subnanometer confined sulfur.^{6,7} In all of these previous studies, it is apparent that the physical confinement of sulfur plays a crucial role in dictating the detailed electrochemical mechanisms in Li–S reactions.

To further study the control over Li–S reactions in confined chemical environments, we utilize single-walled carbon nanotubes (SWNTs) in this study to confine sulfur. SWNTs with nanometer-sized diameters provide an ideal encapsulation host for sulfur because of their intrinsic one-dimensional (1D) confinement within the rigid but electronically conductive SWNT wall. Various materials including fullerenes,^{8–11} inorganic molecules,^{12–16} organic molecular dopants,¹⁷ and metal and metal oxide catalytic nanoparticles^{18,19} have been encapsulated in SWNTs. Recently in 2014, Fujimori et al. proposed that sulfur in a metallic state could be confined in electric arc produced SWNTs (EA-SWNTs) with either linear or zigzag chain structures.²⁰ Based on this proposed S@SWNT structure, Yang et al. studied the electrochemical lithiation-delithiation of sulfur confined in EA-SWNTs,²¹ and their results demonstrated an electrochemical behavior consistent with the typical solution-phase Li–S reaction.

To demonstrate the effects of the confined chemical environment on Li–S reactions, we utilize two types of SWNTs with different diameters, EA-SWNTs (average diameter of 1.55 ± 0.1 nm) and high-pressure carbon monoxide produced SWNTs (HiPco-SWNTs, average diameter of 1.0 ± 0.2 nm), and two different electrolytes: 1 M lithium bis(trifluoromethane sulfonyl)imide (LiTFSI) in tetraethylene glycol dimethyl ether (TEGDME) and 1,4,7,10,13-pentaoxacyclopentadecane (15-crown-5), respec-

tively. Structurally, the 15-crown-5 molecule is the cyclo-counterpart of the linear TEGDME. The selection of these two solvents is based on the rationale that the structures of solvated Li^+ ions in these two solvents differ solely due to the structures of the solvent molecules (linear versus cyclic), thus providing a rigorous comparison of the Li–S electrochemical behavior in the EA-SWNTs and HiPco-SWNTs with distinct diameter sizes. Our findings are complemented by a suite of experimental and computational characterization techniques including *operando* Raman, X-ray photoelectron spectroscopy, and first-principles calculations from density functional theory.

RESULTS AND DISCUSSION

Sulfur was infused into EA-SWNTs and HiPco-SWNTs via exposure to saturated sulfur vapor at 600 °C for 2 days in sealed hourglass-shaped quartz tubes followed by the removal of superficial sulfur (exterior of the SWNTs), as detailed in the **Experimental** section. According to our previous study, S_2 molecules generated at 600 °C can diffuse into the SWNTs and subsequently polymerize to form long-chain sulfur diradicals.²² The sulfur content was determined with elemental analysis via colorimetric titration (**Figure S1**): 4.57 wt % in S@EA and 11.33 wt % in S@HiPco. The sulfur contents were also confirmed by energy-dispersive X-ray spectroscopy analysis (EDX) and electron energy-loss spectroscopy (EELS) (**Figures S2 and S3**). The microstructures of S@EA and S@HiPco were characterized with low-kV monochromated and aberration-corrected high-resolution transmission electron microscopy (HRTEM). As shown in **Figure 1a**, an irregularly shaped sulfur chain can be observed to be folded inside an EA-SWNT with a diameter of 1.5 nm; similarly, a shorter swirl-like sulfur chain can be observed inside a HiPco-SWNT. It is worth mentioning that, despite the low electron-beam energy, the S@SWNTs were unstable under prolonged beam irradiation; as shown in **Figure S4**, a breach of the HiPco-SWNT wall in **Figure 1a** was quickly created by the electron beam, and the sulfur chain escaped. Nevertheless, we observe the sulfur chains confined in the EA- and HiPco-SWNTs do not have a well-defined structure and are distinctly different from the linear or zigzag structures previously proposed. Indeed, our density functional

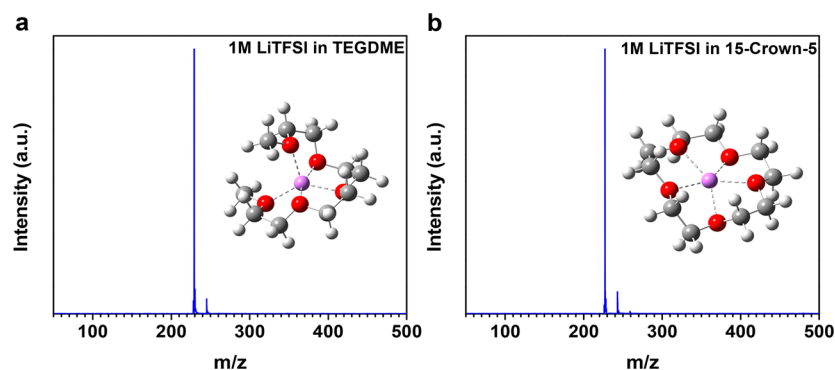


Figure 2. ESI-MS spectra of 1 M LiTFSI in (a) TEGDME and (b) 15-crown-5. The insets of each panel depict the DFT-optimized solvation structures.

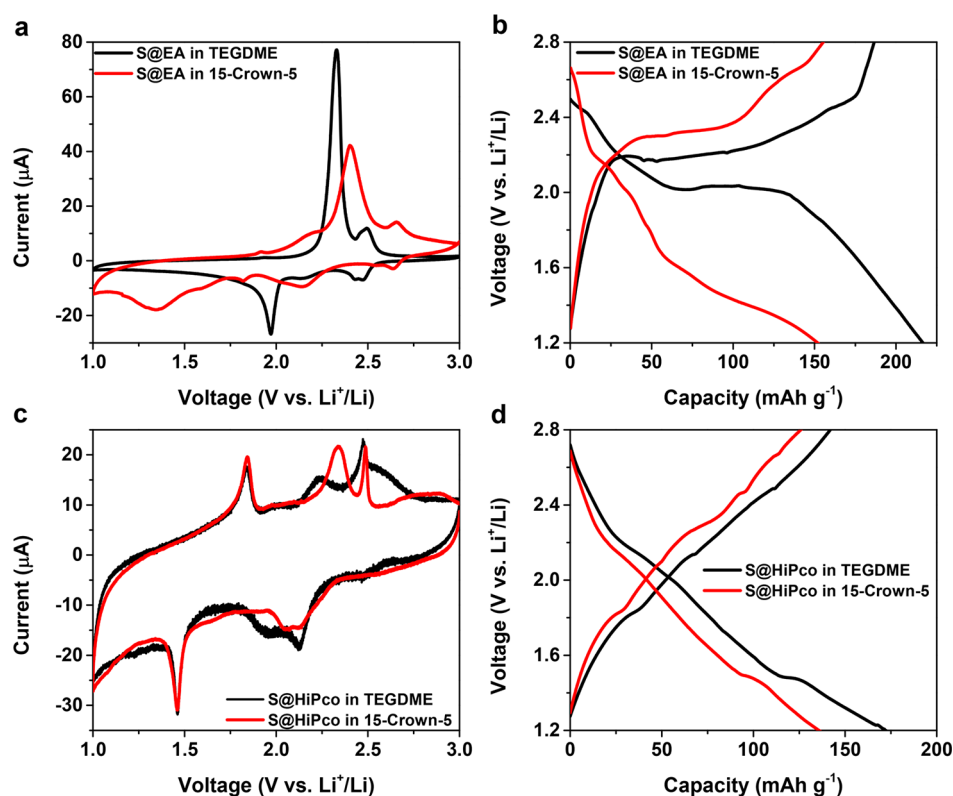


Figure 3. (a) CV and (b) galvanostatic lithiation–delithiation of S@EA in TEGDME and 15-crown-5; (c) CV and (d) galvanostatic lithiation–delithiation of S@HiPco in TEGDME and 15-crown-5. The scan rate of CV is 0.05 mV s^{-1} , and the current density of galvanostatic lithiation–delithiation is 4 mA g^{-1} with respect to the total mass of S@SWNTs. The capacity is also based on the mass of S@SWNTs.

theory (DFT) based calculations demonstrate that a more disordered structure of the sulfur chain is more stable than the linear and zigzag conformations when they are confined in a SWNT.²² In particular, our DFT optimizations depicted in Figure 1b show that the sulfur chain inside the SWNT tends to accommodate conformations that resemble the cyclo- S_8 allotrope, *i.e.*, the bond distances, bond angles, and dihedral angles are similar to the cyclo- S_8 allotrope geometry (see Tables S1–4 for further details and geometric analyses). Our optimized sulfur geometries can be rationalized by recognizing that this allotrope is the most thermodynamically stable form at ambient temperatures.²³

The primary Li^+ ion solvation structures in the electrolytes were characterized with electrospray ionization mass spectrometry (ESI-MS). As shown in Figure 2, the exceptionally

clean ESI-MS spectra of 1 M LiTFSI in TEGDME and 15-crown-5 indicate that the exclusive solvated Li^+ ion species are $[\text{Li}(\text{TEGDME})]^+$ ($m/z = 229.14$) and $[\text{Li}(15\text{-crown-5})]^+$ ($m/z = 227.12$), respectively. The small peaks in the spectra ($m/z = 245.12$ and 243.10 , respectively) can be attributed to the small amount of impurities with one $-\text{OH}$ group instead of H in the solvent molecules. The insets of Figure 2 show the optimized solvation structures of $[\text{Li}(\text{TEGDME})]^+$ and $[\text{Li}(15\text{-crown-5})]^+$ based on DFT calculations. From the optimized solvation structures, the largest van der Waals dimensions of these two solvated Li^+ ions can be estimated by fitting three-dimensional ellipsoid surfaces that enclose all of the DFT-optimized coordinates for each of the solvents. We obtain the largest dimension of 10.87 \AA for $[\text{Li}(\text{TEGDME})]^+$ (ellipsoid axes: $a = 4.56 \text{ \AA}$, $b = 5.12 \text{ \AA}$, and $c = 5.435 \text{ \AA}$) and

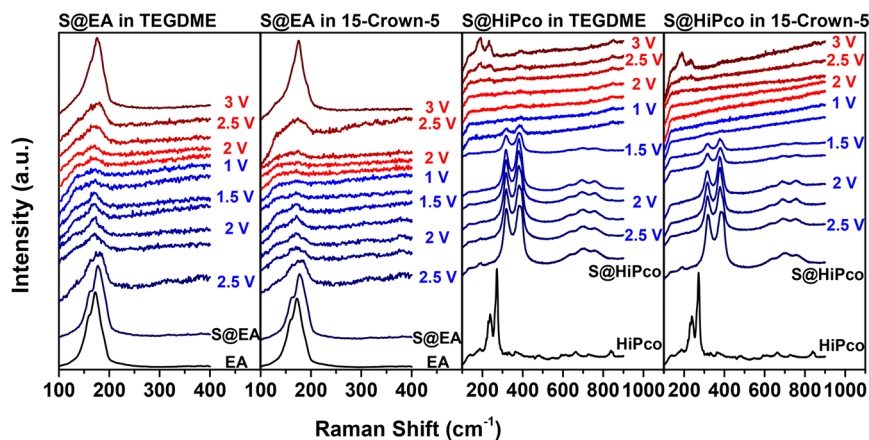


Figure 4. *Operando* Raman spectra showing the RBM region of S@EA and S@HiPco in both TEGDME and 15-crown-5 electrolytes during electrochemical lithiation–delithiation with a current density of 20 mA g⁻¹ with respect to the total mass of S@SWNTs. Lithiation: 2.5 to 1 V. Delithiation: 1 to 3 V vs Li⁺/Li.

11.34 Å for [Li(15-crown-5)]⁺ (ellipsoid axes: $a = 3.51$ Å, $b = 5.24$ Å, and $c = 5.67$ Å), respectively. Therefore, both solvated ions are smaller than the average van der Waals diameter of EA-SWNTs (12.1 Å) but much larger than the average van der Waals diameter of HiPco-SWNTs (6.6 Å).

The electrochemical properties of S@EA and S@HiPco with Li were characterized with CV and galvanostatic lithiation–delithiation in these two electrolytes. Panels a and b of Figure 3 show the CV and galvanostatic lithiation–delithiation curves, respectively, of S@EA in TEGDME and 15-crown-5 electrolytes versus Li⁺/Li. The CV scan in TEGDME electrolyte displays a series of cathodic peaks at 2.45, 2.13, and 1.97 V and two anodic peaks at 2.33 and 2.5 V, which are consistent with its galvanostatic potential profile. The CV scan in 15-crown-5 displays more cathodic peaks at 2.65, 2.15, 1.8, 1.6, and 1.35 V, and correspondingly more anodic peaks at 1.9, 2.2, 2.4, and 2.65 V, which are also consistent with its galvanostatic potential profile. The CV and galvanostatic potential curves of S@EA in TEGDME electrolyte provide strong evidence that S@EA undergoes conventional solution-phase Li–S reactions involving Li polysulfides. The smaller size of solvated [Li(TEGDME)]⁺ ions compared to the EA-SWNTs diameter allows [Li(TEGDME)]⁺ ions to enter the EA-SWNTs with an excess of TEGDME molecules to react with the confined sulfur. In fact, the diameter of the EA-SWNTs is large enough to accommodate both solvated [Li(TEGDME)]⁺ and [Li(15-crown-5)]⁺ ions, enabling the conventional solution-phase Li–S electrochemical reaction in both electrolytes. The seemingly different electrochemical behaviors of Li–S@EA in 15-crown-5 may originate from the much higher viscosity of 15-crown-5 (21.7 cP at 25 °C)²⁴ than that of TEGDME (4.05 cP at 25 °C). The diffusion of Li polysulfides during the electrochemical process can be suppressed by the higher viscosity of 15-crown-5 and the restrictive 1D SWNT confinement. The suppression of Li polysulfide dissolution improves the differentiation of the stepwise charge-transfer processes in sulfur lithiation–delithiation, which typically could not be well distinguished in nonconfined Li–S electrochemical reactions with CV or chronopotentiometry methods.

In sharp contrast, as shown in Figure 3c,d, the electrochemical characteristics of S@HiPco in TEGDME and 15-crown-5 electrolytes are not only fundamentally different from those observed for S@EA but also identical to each other. The CV scans of S@HiPco display four cathodic peaks at 2.5 V

(small in 15-crown-5), 2.12, 1.95, and 1.46 V and three anodic peaks at 1.85 V, 2.23 V (shifted to 2.33 V in 15-crown-5), and 2.48 V, which are consistent with their galvanostatic potential profiles. The identical electrochemical behavior of S@HiPco in TEGDME and 15-crown-5 electrolytes implies identical Li–S electrochemical mechanisms, which cannot be explained by the conventional solution-phase Li–S electrochemical reaction. For comparison, the CV scans of simple sulfur–HiPco–SWNT and sulfur–EA–SWNT mixtures in TEGDME and 15-crown-5 electrolytes display conventional solution-phase Li–S electrochemical behavior as shown in Figure S5. This new mechanism is very likely due to the much smaller diameter of HiPco–SWNTs than that of EA–SWNTs. The inner van der Waals diameter of HiPco–SWNTs is approximately 6.6 Å, which can no longer accommodate either of the solvated [Li(TEGDME)]⁺ and [Li(15-crown-5)]⁺ ions. It is worth noting that the reaction between S@HiPco and Li is apparently different from the ones demonstrated in microporous carbon^{1–3} and with solid-state electrolytes,^{25–27} which are characterized with single slope-like lithiation–delithiation curves and single-pair redox peaks in CV. We hereby propose a new mechanism: the solvated [Li(TEGDME)]⁺ and [Li(15-crown-5)]⁺ ions cannot enter the interior of the HiPco–SWNTs; instead, the sulfur in S@HiPco is reduced through the SWNT wall via an out-of-plane π -electron interaction, with Li⁺ physically outside of SWNT but interacting with the π orbitals of the sp²-carbon.

The *operando* Raman spectroscopy also demonstrates the clear correlation between the Li–S electrochemical reactions and the diameters of the SWNTs. Figure 4 displays the *operando* Raman spectra near the radial breathing mode (RBM) region of SWNTs obtained during the galvanostatic lithiation–delithiation of S@SWNTs in TEGDME and 15-crown-5 electrolytes, respectively. (The full *operando* Raman spectra are shown in Figure S6). Due to the van der Waals interaction between the confined sulfur chains and the wall of the EA-SWNTs, the RBM Raman peak is slightly shifted from 172 cm⁻¹ in EA-SWNTs to 178 cm⁻¹ in S@EA-SWNTs, which is consistent with our previous finding.²² During lithiation, the RBM peak gradually red-shifted back to 172 cm⁻¹ with diminishing intensity. The shift of the peak indicates the weakening van der Waals interaction between the lithiated sulfur and the wall of the EA-SWNTs due to the cleavage of the long sulfur chains. The diminishment of the peak may

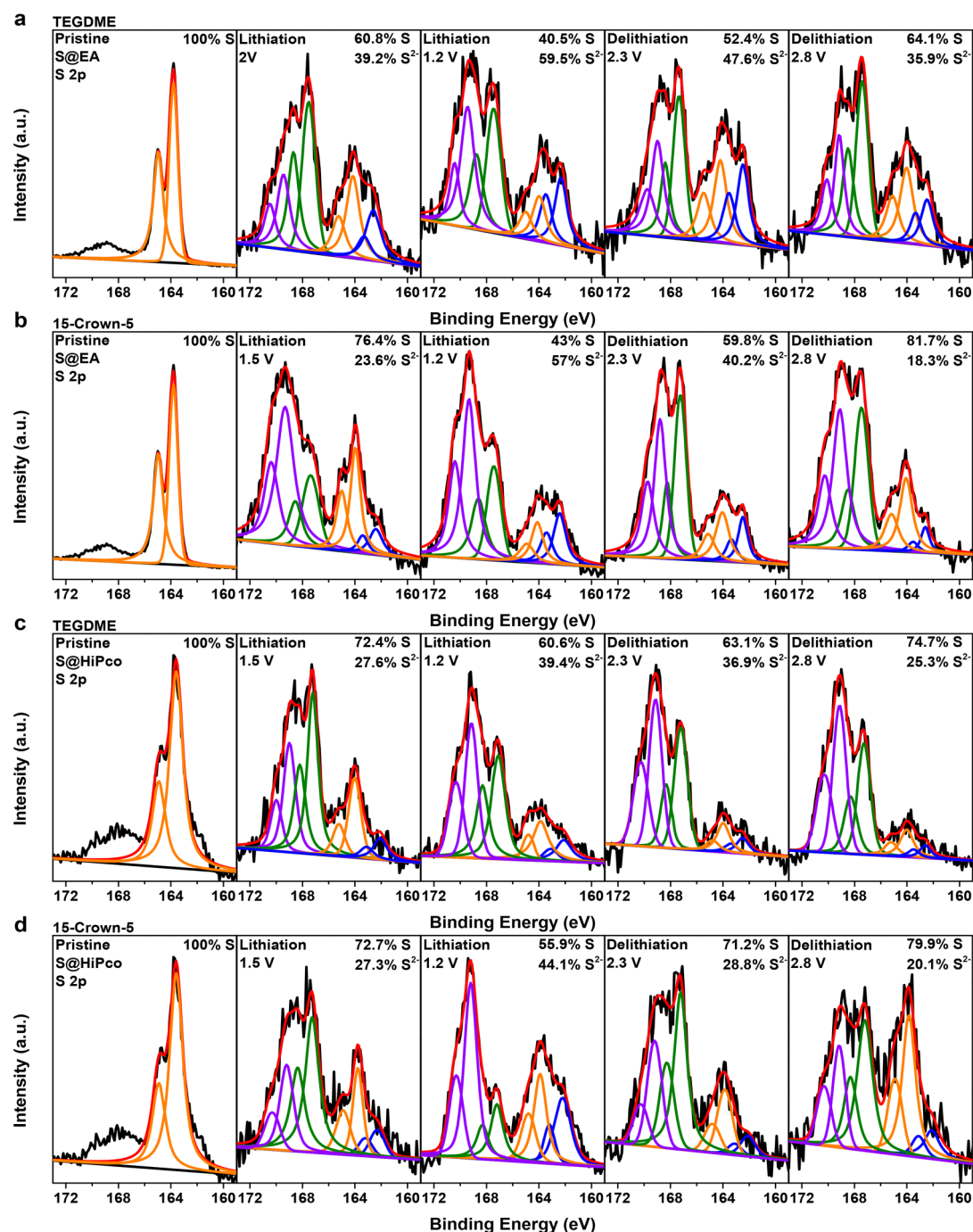


Figure 5. XPS S 2p spectra of (a, b) S@EA and (c, d) S@HiPco at different lithiation–delithiation states in TEGDME and 15-crown-5 electrolytes, respectively. The electrochemical lithiation–delithiation is performed with a current density of 20 mA g^{-1} with respect to the mass of S@EA and S@HiPco. The deconvolution color code is as follows: elemental sulfur peak, orange; oxidized sulfur species peaks, purple and green; Li_2S peak, blue.

indicate the formation of solid electrolyte interphase (SEI) or SEI-like species on the EA-SWNTs, which will be elaborated later in the analysis of the X-ray photoelectron spectroscopy (XPS) data. Another cause for the RBM peak diminishment in EA-SWNTs can be related to the Li to SWNT charge transfer (n-doping) resulting in bleaching of the optical interband transitions in the SWNTs and suppressing the resonance character of the Raman scattering. The reverse process can be observed in the spectra obtained during delithiation. After delithiation to 3 V, the RBM peak blue-shifted to 175 cm^{-1} (lower than 178 cm^{-1} in the pristine S@EA), which indicates

that sulfur was not fully converted back to the long-chain structure in delithiation, resulting in a weaker interaction with the wall of the EA-SWNTs. Interestingly, the RBM peak also became more pronounced during delithiation, which may indicate the diminishing SEI-like species.

The two right panels in Figures 4 depict the *operando* Raman spectra during the lithiation–delithiation of S@HiPco in TEGDME and 15-crown-5 electrolytes, respectively. The sulfur chains confined in HiPco-SWNTs have a stronger van der Waals interaction with the SWNT walls due to the narrower diameter. This results in the disappearance of the

Table 1. Composition of the Sulfur Species in S@EA and S@HiPco Calculated from XPS S 2p Spectra at Different Lithiation–Delithiation States in TEGDME and 15-Crown-5 Electrolytes, Respectively

potential (vs Li ⁺ /Li)		TEGDME					15-crown-5				
		lithiation			delithiation		lithiation			delithiation	
		2.8 V	2.0 V	1.2 V	2.3 V	2.8 V	2.8 V	1.5 V	1.2 V	2.3 V	2.8 V
S@EA	S %	100	60.8	40.5	52.4	64.1	100	76.4	43.0	59.8	81.7
	S ²⁻ %	0	39.2	59.5	47.6	35.9	0	23.6	57.0	40.2	18.3
potential (vs Li ⁺ /Li)		2.8 V	1.5 V	1.2 V	2.3 V	2.8 V	2.8 V	1.5 V	1.2 V	2.3 V	2.8 V
S@HiPco	S %	100	72.4	60.6	63.1	74.7	100	72.7	55.9	71.2	79.9
	S ²⁻ %	0	27.6	39.4	36.9	25.3	0	27.3	44.1	28.8	20.1

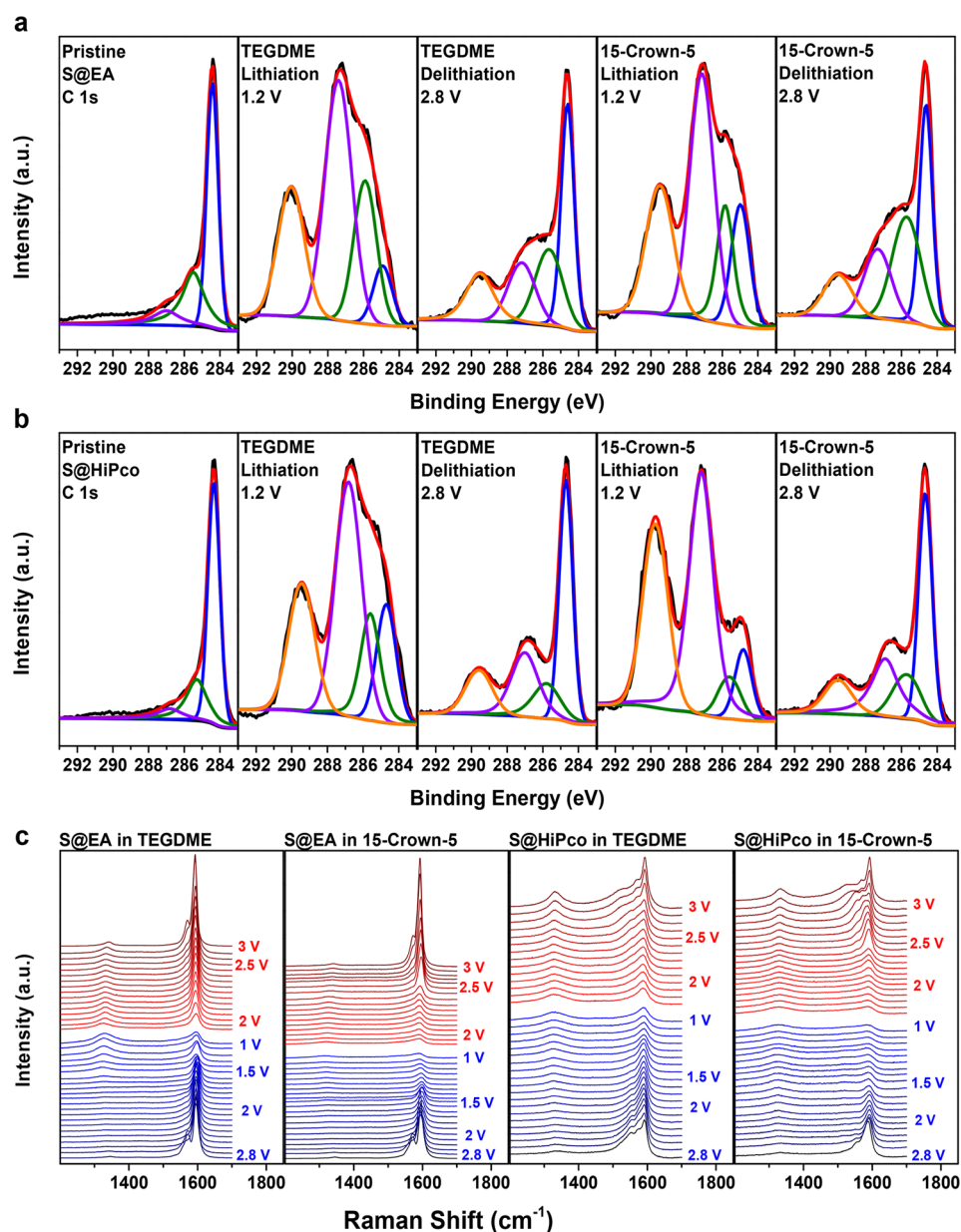


Figure 6. XPS C 1s spectra of (a) pristine S@EA, lithiated, and delithiated S@EA in TEGDME and 15-crown-5 electrolytes and (b) pristine S@HiPco, lithiated, and delithiated S@HiPco in TEGDME and 15-crown-5 electrolytes; (c) *operando* Raman spectra in the D-band and G-band regions of S@EA and S@HiPco during lithiation–delithiation (lithiation, 2.8 to 1 V; delithiation, 1 to 3 V). XPS deconvolution color code: C–C peak, blue; C–O peak, green; C=O peak, purple; O=C–O peak, orange.

RBM peaks at 231 and 272 cm^{-1} and an appearance of new Raman peaks at 315 and 377 cm^{-1} originating from the molecular vibrations of encapsulated sulfur chains coupled with

electronic excitations in SWNTs, as confirmed by the observed ^{32}S to ^{34}S isotopic shift.²² These new Raman peaks of S@HiPco gradually diminished during the lithiation but without a

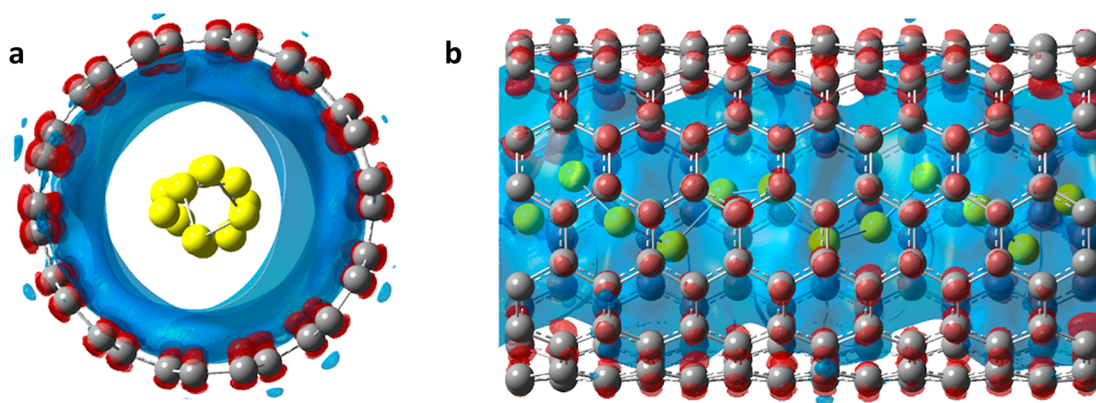


Figure 7. Electron density difference maps ($\Delta\rho = \rho_{S@SWNT} - \rho_{SWNT}$) for a (7,7) S@SWNT viewed along the (a) axis and (b) side length as computed with dispersion-corrected DFT. Red regions denote an accumulation of electron density (compared to the bare SWNT), and blue regions represent a depletion of electron density.

noticeable peak shift. The diminishment of these peaks may be due to the formation of SEI-like species in S@HiPco similar to that observed in S@EA and the suppression of the SWNT interband transitions due to Li-to-SWNT charge transfer.²² The absence of the peak shift may suggest that the reduction of confined sulfur (hypothetically via out-of-plane π -electron interactions) does not alter the interaction with the wall. These new peaks completely disappear at the end of delithiation, while the Raman peaks in the RBM region at 188 and 231 cm^{-1} are partially restored. Although the exact explanation of the Raman peak transformation in S@HiPco is unclear, the different *operando* Raman spectra can be unambiguously attributed to the narrower diameter of the HiPco-SWNTs than EA-SWNTs.

The S@EA and S@HiPco at different states of lithiation-delithiation in TEGDME and 15-crown-5 electrolytes were further characterized with XPS. As shown in Figure 5, the S 2p spectra of pristine S@EA and S@HiPco both display S 2p_{3/2} and S 2p_{1/2} peaks of elemental sulfur at 164 and 165.2 eV. A small amount of the oxidized sulfur assigned to the peaks in the range of 166 to 171 eV in the pristine samples could be introduced during the sulfur infusion processes. The peaks of oxidized sulfur became more pronounced in the lithiated and delithiated samples due to the LiTFSI residue and possible [TFSI]⁻ anion decomposition.^{28–30} The XPS spectra indicate that all the lithiated and delithiated S@SWNTs contain two sulfur species: elemental sulfur and lithium sulfide. These two species have different ratios at different lithiation-delithiation states, as listed in Table 1. It is worth noting that due to the spontaneous disproportionation of Li polysulfides to elemental sulfur and Li₂S upon solvent removal,^{31,32} the ratio of S to S²⁻ obtained from the *ex situ* XPS of S@EA only reflects the extent of lithiation-delithiation, not necessarily the actual products in the electrochemical environmental. However, the sulfur and Li₂S species detected in S@HiPco are expectedly the actual products based on the proposed reactions in S@HiPco via out-of-plane π electron interactions without polysulfides.

The most salient results from the S-to-S²⁻ ratio in the XPS is that the capacity of S@EA and S@HiPco shown in Figure 3 cannot be solely attributed to the lithiation-delithiation of sulfur. Based on the sulfur conversion in S@HiPco, the capacity contributed from sulfur lithiation is 82 mAh g⁻¹ in TEGDME and 78 mAh g⁻¹ in 15-crown-5, suggesting that about 50% of the demonstrated capacity originates from a different mechanism (Figure 3d). The extra capacity in S@EA

is also significant: the lithiation of sulfur only contributes 45 mAh g⁻¹ to the total capacity of 190 mAh g⁻¹ in TEGDME and 44 mAh g⁻¹ to the total capacity of 152 mAh g⁻¹ in 15-crown-5 (Figure 3b). The extra capacity does not originate from the lithiation-delithiation of neat EA-SWNTs and HiPco-SWNTs, which displays negligible capacity (Figure S7). The *ex situ* XPS C 1s spectra of the lithiated and delithiated S@EA and S@HiPco sheds some light on the origin of the extra capacity: as shown in Figure 6a,b, the spectra of the pristine S@EA and S@HiPco both indicate the existence of a C–C bond at 284.5 eV (blue curve), a C–O bond at 285.5 eV (green curve), and an isolated carbonyl C=O bond at 287 eV (purple curve). The latter two may arise from the impurity of the pristine SWNTs or impurities introduced during the sulfur encapsulation. During lithiation, both C–O and C=O peaks become much more pronounced by using the C–C peak at 284.5 eV as a reference. In addition, a strong peak representing a carboxylic acid ester group (O=C–O) appears at 289.5 eV (orange) in lithiation. This observation indicates the formation of possible species including C–O–Li and O=C–O–Li due to the TEGDME and 15-crown-5 decomposition via electrochemical reduction in the presence of Li⁺ ions.^{33,34} These observations are consistent with the indication from the *operando* Raman results displayed in Figure 6c. Both S@EA and S@HiPco in either electrolyte clearly demonstrate decreasing the G-band peak (1580 cm^{-1}) and increasing the D-band peak (1350 cm^{-1}) during lithiation and the reverse trend during delithiation. Such reactions apparently do not occur under the same condition with pure EA-SWNTs and HiPco-SWNTs. Therefore, S@EA and S@HiPco nanostructures may possess catalytic activity to facilitate the formation of these species. After delithiation, the intensity of the peaks at 289.5 eV (O=C–O–Li), 287 eV (C=O), and 285.5 (C–O–Li) all significantly decrease in comparison to the C–C peak at 284.5 eV, which suggests the decomposition of the SEI-like layer under an electrochemical oxidation environment. The reversibility of these SEI-like species was still observed after 10 cycles in the XPS C 1s spectra (Figure S8).

The reversible formation and decomposition of the SEI-like layer, facilitated by the hypothesized catalytic activity of S@EA and S@HiPco, clearly contribute to the extra capacity during lithiation-delithiation. Indeed, our large-scale DFT calculations on these nanostructures corroborate the proposed catalytic activity by showing that a significant dynamic electron

transfer occurs from the encapsulated sulfur to the surrounding SWNT and electrolyte. Figure 7 depicts the electron density difference ($\Delta\rho = \rho_{S@SWNT} - \rho_{SWNT}$)³⁵ for a (7,7) S@SWNT computed with dispersion-corrected DFT.³⁶ As depicted in Figure 7, $\Delta\rho$ gives a dynamic visualization of electronic rearrangement when sulfur is encapsulated within the SWNT: red regions denote an accumulation of electron density (primarily around the SWNT), and blue regions represent a depletion of density (from the sulfur). The amount of charge transfer is quite sizable with 0.37 e⁻ being transferred from the sulfur to the SWNT within the unit cell depicted in Figure 7. Most notably, our DFT calculations show similar trends with other SWNT chiralities [such as the (10,0) semiconducting SWNT] as well as S@SWNT geometries in the presence of a surrounding electrolyte (Figure S9).

CONCLUSIONS

In summary, we have investigated the chemical properties of sulfur confined in EA-SWNTs and HiPco-SWNTs, and we demonstrate an unusual electrochemical reactivity of sulfur upon encapsulation in narrow-diameter (sub-nanoscale) SWNTs with lithium. Our findings are corroborated and supported with various spectroscopic analyses including *operando* Raman, X-ray photoelectron spectroscopy, and first-principles calculations from density functional theory. Collectively, these results show that electrochemical properties can be dramatically modulated by varying the diameter of the SWNTs and the dimension of the solvated Li⁺ ions. Specifically, the relatively large diameter of EA-SWNTs accommodates solvated Li⁺ ions so that solution-phase Li–S reactions can occur within the interior of EA-SWNTs. In contrast, the narrower diameter of HiPco-SWNTs prevents solvated Li⁺ ions from entering the interior. As a result, the Li–S reaction in HiPco-SWNTs is markedly different and proposed to occur via a through-wall π electron interaction. Our combined spectroscopic and DFT analyses also suggest a formation-decomposition mechanism of SEI-like species facilitated by the catalytic activity of the S@SWNTs, which is induced by the sulfur–SWNT interactions in this nanochemical environment. This finding provides an exciting opportunity that can be further leveraged to probe fundamental chemical reaction mechanisms of S@SWNTs as energy storage or electrocatalytic materials.

EXPERIMENTAL SECTION

Preparation of S@SWNTs. SWNTs (EA-SWNTs obtained from Carbon Solutions, Inc. and HiPco-SWNTs purchased from Nano-Integris) and sulfur (99.99%, Sigma-Aldrich) were sealed in a vacuum hourglass-shaped quartz tube as shown in Figure S10. SWNTs were loaded in the top compartment, and sulfur was loaded in the bottom one. The sealed tube was placed vertically in a muffle furnace for heat treatment at 600 °C for 48 h. Under the experimental conditions, the sulfur in the sealed tube reached vapor–liquid phase equilibrium. Therefore, the SWNTs were exposed to saturated sulfur vapor without contact with liquid sulfur. After the heat treatment, the obtained materials were further heated at 350 °C in flowing argon for 10 h to completely remove the sulfur deposited on the exterior of SWNTs.

Microscopic Characterization. The samples were dispersed in dimethylformamide (DMF) by ultrasonication with a 5 s pulse on and a 10 s pulse off at room temperature for 2 h and then dropped onto TEM grids. HRTEM imaging was performed on an aberration-corrected and monochromated G2 cubed Titan 60–300 electron microscope under 60 kV. Scanning transmission electron microscopy

(STEM) was performed with an aberration-corrected Nion Ultra-STEM 100 at Oak Ridge National Laboratory, which is equipped with a second generation fifth-order probe aberration corrector, a cold field emission electron gun, and a Gatan Enfina energy loss spectrometer. Imaging was performed at 60 keV, below the knock-on threshold for carbon atoms, to minimize damage on SWNTs using a semi-convergence angle of 30 mrad and an inner semi-angle of 54 mrad for the annular dark-field detector. EEL spectroscopy and spectrum imaging was performed simultaneously with imaging and with a dispersion of 0.1 eV per channel.

Electrochemical Characterization. The electrodes were composed of 90 wt % of S@SWNTs (or pure SWNTs) and 10 wt % of polyvinylpyrrolidone (Sigma-Aldrich) binder. The areal loading of S@SWNTs or pure SWNTs is approximately 2 mg cm⁻². Aluminum foil (99.45%, Alfa Aesar) was used as the current collector. Two-electrode coin cells with lithium foil (Alfa Aesar) as the counter electrode were assembled in an argon-filled glovebox for the electrochemical analysis. Electrolytes consisting of 1 M LiTFSI (Sigma-Aldrich) in TEGDME (Sigma-Aldrich) and 15-crown-5 (Sigma-Aldrich) were used with a porous membrane separator (Celgard 2500). The cells were charged and discharged with different cycling currents between 1 and 3 V (vs Li⁺/Li) using an Arbin battery test station. CV scans were performed on a Gamry Interface 1000 analyzer.

Operando Raman Spectroscopy. S@SWNTs (2 mg) were dispersed in 100 mL of DMF by sonication for 5 h. The dispersion was centrifuged at 8000 rpm (11000g) for 15 min. The obtained supernatant was then filtered through a porous membrane (Celgard 2500), which was also used as the separator in the cells for the *operando* Raman study. The S@SWNTs film coated membrane (Figure S11) was used as the positive electrode in the modified cell for *Operando* Raman measurement. A coin cell case with a Kapton window on the positive side was purchased from MTI Corporation. The Kapton film was cut off, and a thin transparent glass slide was attached on the cell case using Frame-Seal tape (Biorad). The cells were assembled in an argon-filled glovebox with the S@SWNTs film facing the glass window (Figure S12). The cells were mounted onto a Raman microscope (Nicolet Almega XR with 532 nm wavelength laser source) with the window facing the laser source. The cells were lithiated and delithiated at a current density of 20 mA g⁻¹ with a Gamry Reference 3000 analyzer, while the Raman spectra was collected every 10 min.

X-ray Photoelectron Spectroscopy. The cells were discharged or charged to a certain potential and disassembled in an argon-filled glovebox. The S@SWNTs electrodes were washed with dimethoxyethane 3 times to remove the electrolyte residual and dried at room temperature in the glovebox for 48 h. The chemical state of sulfur and carbon in the S@SWNTs was characterized with XPS (AXIS Supra) at the Irvine Materials Research Institute at University of California Irvine. An inert gas-filled glovebox is attached to the Supra's ultrahigh-vacuum preparation chamber so the samples were not exposed to the ambient environment.

DFT Computational Methods. Geometry optimizations of a (7,7) SWCNT filled with sulfur were carried out with the VASP code using a plane-wave basis and periodic boundary conditions, in which the projector augmented wave method was used to numerically represent the electron wave functions. We used the non-local optB86b-vdW exchange-correlation functional, which explicitly calculates van der Waals effects (via non-local double real-space integrals of the electron density) to account for the dispersion interactions between the SWNT and the sulfur chain. A 4 × 1 × 1 mesh of *k* points was implemented for the Brillouin zone integration, and a 402 eV energy cut-off was used for the electronic wave functions. A vacuum region of ~30 Å was used in the *y* and *z* directions, and periodic boundary conditions were applied in all three dimensions.

ASSOCIATED CONTENT

Supporting Information

The Supporting Information is available free of charge on the ACS Publications website at DOI: 10.1021/acsnano.7b08778.

Sulfur content analysis, EDX and EELS results, additional HRTEM images, DFT optimizations and geometric analyses, CV of a simple mixture of sulfur with EA-SWNTs and HiPco-SWNTs, full *operando* Raman spectra, galvanostatic lithiation–delithiation, XPS C 1s spectra, DFT S@SWNT geometries, digital images of the vacuum vessel for sulfur infusion, S@SWNT electrode, and modified the cell for *operando* Raman experiments (PDF)

AUTHOR INFORMATION

Corresponding Authors

*E-mail: jguo@engr.ucr.edu.

*E-mail: bryan.wong@ucr.edu.

ORCID

M. Belén Oviedo: 0000-0002-3200-9929

Mikhail E. Itkis: 0000-0003-2447-2267

Miaofang Chi: 0000-0003-0764-1567

Yu Han: 0000-0003-1462-1118

Bryan M. Wong: 0000-0002-3477-8043

Juchen Guo: 0000-0001-9829-1202

Notes

The authors declare no competing financial interest.

ACKNOWLEDGMENTS

XPS work was performed at the UC Irvine Materials Research Institute (IMRI) using instrumentation funded in part by the National Science Foundation Major Research Instrumentation Program under grant no. CHE-1338173. M.B.O. and B.M.W. acknowledge the National Science Foundation for the use of supercomputing resources through the Extreme Science and Engineering Discovery Environment (XSEDE), project no. TG-ENG160024. Electron microscopy work (EELS) was conducted as part of a user project at ORNL's Center for Nanophase Materials Sciences (CNMS), which is sponsored by the Scientific User Facilities Division, Office of Basic Energy Sciences, U.S. Department of Energy. B.M.W. and J.G. acknowledge the National Science Foundation for financial support under grant no. CBET-1604908.

DEDICATION

This work is dedicated to our dear colleague and friend, Prof. Robert C. Haddon.

REFERENCES

- (1) Fu, C. Y.; Wong, B. M.; Bozhilov, K. N.; Guo, J. C. Solid State Lithiation-delithiation of Sulphur in Sub-nano Confinement: A New Concept for Designing Lithium-Sulphur Batteries. *Chem. Sci.* **2016**, *7*, 1224–1232.
- (2) Wang, D.-W.; Zhou, G. M.; Li, F.; Wu, K.-H.; Lu, G. M.; Cheng, H.-M.; Gentle, I. A. Microporous-Mesoporous Carbon with Graphitic Structure for a High-Rate Stable Sulfur Cathode in Carbonate Solvent-Based Li-S Batteries. *Phys. Chem. Chem. Phys.* **2012**, *14*, 8703–8710.
- (3) Li, Z.; Yuan, L.; Yi, Z.; Sun, Y.; Liu, Y.; Jiang, Y.; Shen, Y.; Xin, Y.; Zhang, Z.; Huang, Y. Insight into the Electrode Mechanism in Lithium-Sulfur Batteries with Ordered Microporous Carbon Confined Sulfur as the Cathode. *Adv. Energy Mater.* **2014**, *4*, 1301473.

- (4) Xin, S.; Gu, L.; Zhao, N.-H.; Yin, Y.-X.; Zhou, L.-J.; Guo, Y.-G.; Wan, L.-J. Smaller Sulfur Molecules Promise Better Lithium-Sulfur Batteries. *J. Am. Chem. Soc.* **2012**, *134*, 18510–18513.

- (5) Zhang, S. S. Sulfurized Carbon: A Class of Cathode Materials for High Performance Lithium/Sulfur Batteries. *Front. Energy Res.* **2013**, *1*, 1–9.

- (6) Markevich, E.; Salitra, G.; Rosenman, A.; Talyosef, Y.; Chesneau, F.; Aurbach, D. The Effect of A Solid Electrolyte Interphase on the Mechanism of Operation of Lithium-Sulfur Batteries. *J. Mater. Chem. A* **2015**, *3*, 19873–19883.

- (7) Markevich, E.; Salitra, G.; Talyosef, Y.; Chesneau, F.; Aurbach, D. Review—On the Mechanism of Quasi-Solid-State Lithiation of Sulfur Encapsulated in Microporous Carbons: Is the Existence of Small Sulfur Molecules Necessary? *J. Electrochem. Soc.* **2017**, *164*, A6244–A6253.

- (8) Smith, B. W.; Monthieux, M.; Luzzi, D. E. Encapsulated C60 in Carbon Nanotubes. *Nature* **1998**, *396*, 323–324.

- (9) Kataura, H.; Maniwa, Y.; Kodama, T.; Kikuchi, K.; Hirahara, K.; Suenaga, K.; Iijima, S.; Suzuki, S.; Achiba, Y.; Krätschmer, W. High-Yield Fullerene Encapsulation in Single-Wall Carbon Nanotubes. *Synth. Met.* **2001**, *121*, 1195–1196.

- (10) Monthieux, M. Filling Single-Wall Carbon Nanotubes. *Carbon* **2002**, *40*, 1809–1823.

- (11) Khlobystov, A. N.; Britz, D. A.; Briggs, G. A. D. Molecules in Carbon Nanotubes. *Acc. Chem. Res.* **2005**, *38*, 901–909.

- (12) Medeiros, P. V. C.; Marks, S.; Wynn, J. M.; Vasylenko, A.; Ramasse, Q. M.; Quigley, D.; Sloan, J.; Morris, A. J. Single-Atom Scale Structural Selectivity in Te Nanowires Encapsulated Inside Ultranarrow, Single-Walled Carbon Nanotubes. *ACS Nano* **2017**, *11*, 6178–6185.

- (13) Hart, M.; White, E. R.; Chen, J.; McGilvery, C. M.; Pickard, C. J.; Michaelides, A.; Sella, A.; Shaffer, M. S. P.; Salzmann, C. G. Encapsulation and Polymerization of White Phosphorus Inside Single-Wall Carbon Nanotubes. *Angew. Chem., Int. Ed.* **2017**, *56*, 8144–8148.

- (14) Komsa, H.-P.; Senga, R.; Suenaga, K.; Krashenninnikov, A. V. Structural Distortions and Charge Density Waves in Iodine Chains Encapsulated inside Carbon Nanotubes. *Nano Lett.* **2017**, *17*, 3694–3700.

- (15) Botos, A.; Biskupek, J.; Chamberlain, T. W.; Rance, G. A.; Stoppello, C. T.; Sloan, J.; Liu, Z.; Suenaga, K.; Kaiser, U.; Khlobystov, A. N. Carbon Nanotubes as Electrically Active Nanoreactors for Multi-Step Inorganic Synthesis: Sequential Transformations of Molecules to Nanoclusters and Nanoclusters to Nanoribbons. *J. Am. Chem. Soc.* **2016**, *138*, 8175–8183.

- (16) Eliseev, A. A.; Chernysheva, M. V.; Verbitskii, N. L.; Kiseleva, E. A.; Lukashin, A. V.; Tretyakov, Y. D.; Kiselev, N. A.; Zhigalina, O. M.; Zakalyukin, R. M.; Vasiliev, A. L.; Krestinin, A. V.; Hutchison, J. L.; Freitag, B. Chemical Reactions within Single-Walled Carbon Nanotube Channels. *Chem. Mater.* **2009**, *21*, 5001–5003.

- (17) Takenobu, T.; Takano, T.; Shiraishi, M.; Murakami, H.; Ata, M.; Kataura, H.; Achiba, Y.; Iwasa, Y. Stable and Controlled Amphoteric Doping by Encapsulation of Organic Molecules inside Carbon Nanotubes. *Nat. Mater.* **2003**, *2*, 683–688.

- (18) Castillejos, E.; Debouttière, P. J.; Roiban, L.; Solhy, A.; Martinez, V.; Kihn, Y.; Ersen, O.; Philippot, K.; Chaudret, B.; Serp, P. An Efficient Strategy to Drive Nanoparticles into Carbon Nanotubes and the Remarkable Effect of Confinement on Their Catalytic Performance. *Angew. Chem.* **2009**, *121*, 2567–2571.

- (19) Pan, X.; Bao, X. The Effects of Confinement inside Carbon Nanotube on Catalysis. *Acc. Chem. Res.* **2011**, *44*, 553–650.

- (20) Fujimori, T.; Morelos-Gómez, A.; Zhu, Z.; Muramatsu, H.; Futamura, R.; Urita, K.; Terrones, M.; Hayashi, T.; Endo, M.; Hong, S. Y.; et al. Conducting Linear Chains of Sulphur Inside Carbon Nanotubes. *Nat. Commun.* **2013**, *4*, 3162.

- (21) Yang, C.-P.; Yin, Y.-X.; Guo, Y.-G.; Wan, L.-J. Electrochemical (De)Lithiation of 1D Sulfur Chains in Li–S Batteries: A Model System Study. *J. Am. Chem. Soc.* **2015**, *137*, 2215–2218.

(22) Li, G.; Fu, C.; Oviedo, M. B.; Chen, M.; Tian, X.; Bekyarova, E.; Itkis, M. E.; Wong, B. M.; Guo, J.; Haddon, R. C. Giant Raman Response to the Encapsulation of Sulfur in Narrow Diameter Single-Walled Carbon Nanotubes. *J. Am. Chem. Soc.* **2016**, *138*, 40–43.

(23) Greenwood, N. N.; Earnshaw, A. *Chemistry of the Elements*, 2nd ed.; Butterworth-Heinemann: Oxford, England, 1997.

(24) Weast, R. C.; Astle, M. J. *CRC Handbook of Chemistry and Physics*, 62nd ed.; CRC Press: Boca Raton, FL, 1981.

(25) Lin, Z.; Liu, Z.; Dudney, N. J.; Liang, C. Lithium Superionic Sulfide Cathode for All-Solid Lithium–Sulfur Batteries. *ACS Nano* **2013**, *7*, 2829–2833.

(26) Lin, Z.; Liu, Z.; Fu, W.; Dudney, N. J.; Liang, C. Lithium Polysulfidophosphates: A Family of Lithium-Conducting Sulfur-Rich Compounds for Lithium–Sulfur Batteries. *Angew. Chem., Int. Ed.* **2013**, *52*, 7460–7463.

(27) Han, F.; Yue, J.; Fan, X.; Gao, T.; Luo, C.; Ma, Z.; Suo, L.; Wang, C. High-Performance All-Solid-State Lithium–Sulfur Battery Enabled by a Mixed-Conductive Li_2S Nanocomposite. *Nano Lett.* **2016**, *16*, 4521–4527.

(28) Fu, Y.; Zu, C.; Manthiram, A. *In Situ*-formed Li_2S in Lithiated Graphite Electrodes for Lithium–Sulfur Batteries. *J. Am. Chem. Soc.* **2013**, *135*, 18044–18047.

(29) Su, Y.-S.; Fu, Y.; Cochell, T.; Manthiram, A. A Strategic Approach to Recharging Lithium–Sulphur Batteries for Long Cycle Life. *Nat. Commun.* **2013**, *4*, 2985–2992.

(30) Tao, X.; Wang, J.; Ying, Z.; Cai, Q.; Zheng, G.; Gan, Y.; Huang, H.; Xia, Y.; Liang, C.; Zhang, W.; Cui, Y. Strong Sulfur Binding with Conducting Magnéli-Phase $\text{Ti}_n\text{O}_{2n-1}$ Nanomaterials for Improving Lithium–Sulfur Batteries. *Nano Lett.* **2014**, *14*, 5288–5294.

(31) Sharma, R. A. Equilibrium Phases in the Lithium–Sulfur System. *J. Electrochem. Soc.* **1972**, *119*, 1439–1443.

(32) Cunningham, P. T.; Johnson, S. A.; Cairns, E. J. Phase Equilibria in Lithium–Chalcogen Systems II. Lithium–Sulfur. *J. Electrochem. Soc.* **1972**, *119*, 1448–1450.

(33) Islam, M. M.; Bryantsev, V. S.; van Duin, A. C. T. ReaxFF Reactive Force Field Simulations on the Influence of Teflon on Electrolyte Decomposition during Li/SWCNT Anode Discharge in Lithium–Sulfur Batteries. *J. Electrochem. Soc.* **2014**, *161*, E3009–E3014.

(34) Assary, R. S.; Curtiss, L. A.; Moore, J. S. Toward a Molecular Understanding of Energetics in Li–S Batteries Using Nonaqueous Electrolytes: A High-Level Quantum Chemical Study. *J. Phys. Chem. C* **2014**, *118*, 11545–11558.

(35) Wong, B. M.; Hsieh, T. H. Optoelectronic and Excitonic Properties of Oligoacenes: Substantial Improvements from Range-Separated Time-Dependent Density Functional Theory. *J. Chem. Theory Comput.* **2010**, *6*, 3704–3712.

(36) Joo, Y.; Kim, M.; Huang, P.; Kanimozhi, C.; Wong, B. M.; Roy, S. S.; Arnold, M. S.; Gopalan, P. Effect of Dipolar Molecule Structure on the Mechanism of Graphene-Enhanced Raman Scattering. *J. Phys. Chem. C* **2016**, *120*, 13815–13824.